

# Magnetic Correlation Spectroscopy in CrSBr

Lukas Krelle,<sup>1</sup> Ryan Tan,<sup>1</sup> Daria Markina,<sup>1</sup> Priyanka Mondal,<sup>1</sup> Kseniia Mosina,<sup>2</sup> Kevin Hagmann,<sup>1</sup> Regine von Klitzing,<sup>1</sup> Kenji Watanabe,<sup>3</sup> Takashi Taniguchi,<sup>4</sup> Zdenek Sofer,<sup>2</sup> and Bernhard Urbaszek<sup>1,\*</sup>

<sup>1</sup>*Institute for Condensed Matter Physics, TU Darmstadt,  
Hochschulstraße 6-8, D-64289 Darmstadt, Germany*

<sup>2</sup>*Department of Inorganic Chemistry, University of Chemistry and  
Technology Prague, Technická 5, 166 28 Prague 6, Czech Republic*

<sup>3</sup>*Research Center for Electronic and Optical Materials,  
National Institute for Materials Science, 1-1 Namiki, Tsukuba 305-0044, Japan*

<sup>4</sup>*Research Center for Materials Nanoarchitectonics,  
National Institute for Materials Science, 1-1 Namiki, Tsukuba 305-0044, Japan*

(Dated: March 12, 2025)

CrSBr is an air-stable magnetic van der Waals semiconductor with strong magnetic anisotropy, where the interaction of excitons with the magnetic order enables the optical identification of different magnetic phases. Here, we study the magnetic anisotropy of multi-layer CrSBr inside a three-axis vector magnet and correlate magnetic order and optical transitions in emission and absorption. We identify layer by layer switching of the magnetization through drastic changes of the optical emission and absorption energy and strength as a function of the applied magnetic field. We correlate optical transitions in reflection spectra with photoluminescence (PL) emission using a transfer-matrix analysis and find that ferromagnetic and antiferromagnetic order between layers can coexist in the same crystal. In the multi-peak PL emission the intensity of energetically lower lying transitions reduces monotonously with increasing field strength whereas energetically higher lying transitions around the bright exciton  $X_B$  brighten close to the saturation field. Using this contrasting behavior we can therefore correlate transitions with each other.

## I. INTRODUCTION

Due to a plethora of tunable magnetic intra- and interlayer interactions [1] layered magnetic materials have motivated research towards applications in data storage [2, 3] and spintronics [4, 5]. However, many layered magnetic semiconductors like the chromium trihalides and related materials suffer from instability under ambient conditions [6–9]. The semiconducting layered antiferromagnet CrSBr overcomes this problem as a stable material in ambient conditions [10, 11]. It is well suited for fundamental studies of magnons [12–14], exciton-phonon coupling [15–17], exciton-photon coupling [18–22] as well as applications in magnetic devices exhibiting large negative magnetoresistance [23, 24], tunable properties with magnetic fields [25] and electrostatic doping [26]. CrSBr crystals are strongly anisotropic which results in strong dependence on the crystallographic axes also for magnetic, optical and electronic properties [25, 27, 28].

The strong coupling between excitons and the magnetic order in CrSBr enables the spectroscopic identification of different magnetic phases [25, 26, 29] as well as spatial domains [26]. The spectroscopic signature of excitonic transitions is not limited to the topmost layer but also reveals information about deeper lying layers [30], which is potentially an advantage compared to successful scanning probe techniques [31, 32]. Up to now, research has mainly focused on understanding the magnetic and exci-

tonic properties of bulk systems and single to 4 layer systems. However, the study of multilayer systems, which exhibit complex emission properties without the influence of strong exciton-photon coupling, has remained elusive.

In this work, we study the anisotropic magnetic properties of CrSBr inside a vector magnet at cryogenic temperatures. We use correlated spectral changes occurring with application of a magnetic field to investigate the origin and connections of several emission lines present in multilayer samples of CrSBr. To this end, we fabricated two multilayer samples, one (14 layers, thickness determined by atomic force microscopy  $11.3 \pm 0.2$  nm) encapsulated in hBN, another one as-exfoliated (10 layers, thickness determined by atomic force microscopy  $8.2 \pm 0.3$  nm). We performed magnetic field dependent photoluminescence (PL) and differential reflectance contrast (DR/R) measurements at  $T = 4.7$  K and carefully track emission energy and intensity to conclude on potential emission origins. Our measurements show, that the ferromagnetic state is reached gradually throughout the crystal as different layers switch from the antiferromagnetic to the ferromagnetic order at different fields. We find phases close to the saturation field, that show a superposition of spectral signatures of both the ferromagnetic (FM) and antiferromagnetic (AFM) state.

## II. RESULTS AND DISCUSSION

We performed cryogenic magneto-optical spectroscopy inside a three-axis vector magnet, in which the crystal-

\*Electronic address: [bernhard.urbaszek@pkm.tu-darmstadt.de](mailto:bernhard.urbaszek@pkm.tu-darmstadt.de)

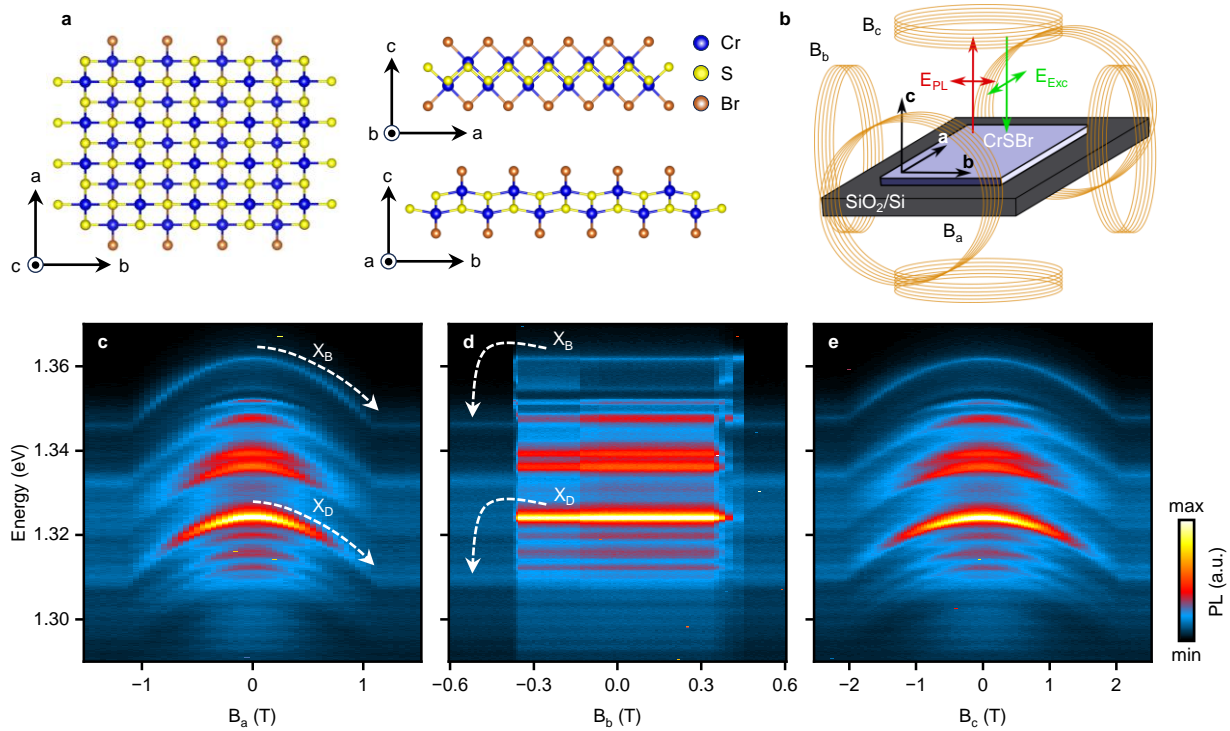


FIG. 1: **Experiments on CrSBr in three-axis vector magnet** a: CrSBr crystal structure. Crystallographic axes a,b,c are indicated by arrows. b: Sketch of a CrSBr sample inside the vector magnet and the orientation of Laser and PL polarization with respect to crystallographic axes. c-e: Exemplary PL magnetic field sweeps of the encapsulated sample for the same spatial spot along the crystal a-,b- and c-axis respectively displaying the magnetic anisotropy, where  $B_a \parallel a$ ,  $B_b \parallel b$  and  $B_c \parallel c$ . Dashed white arrows are a guide for the eye for evolution of  $X_D$  (at 1.324 eV at  $B=0$ ) and  $X_B$  (at 1.362 eV at  $B=0$ ) transitions.

lographic axes are aligned with the magnetic field axes. Figures 1 a and b display the crystal structure of CrSBr and the experimental configuration respectively. Unless noted differently, we focus on the hBN encapsulated 14 layer sample. We performed PL measurements at  $T = 4.7$  K with an excitation energy of 1.959 eV, above the estimated band gap of CrSBr [25, 27]. First, we study the magnetic anisotropy of the material, which is clearly visible in the magnetic field sweeps along the crystal axes shown in Figure 1 c-e for the same sample spot. At zero magnetic field, below the critical temperature, the layers show PL spectra associated with antiferromagnetic order, as spins in adjacent layers point in the opposite direction along the crystal b-axis [11, 33, 34]. The application of a magnetic field rotates the magnetization such that beyond a certain saturation field, all layers are magnetized along the same direction (i.e. parallel to the applied field) corresponding to ferromagnetic order. We trace the change from AFM to FM order through changes in the PL energy [25]. For magnetic fields applied along the magnetic hard (c-axis) and the magnetic intermediate axis (a-axis), the spins rotate gradually while for magnetic fields applied along the magnetic easy axis (b-axis), the spins flip abruptly [25]. The saturation fields along the different axis for the data shown are, respectively  $B_c^s = \pm 2.05 \pm 0.05$  T and  $B_a^s = \pm 1.10 \pm 0.05$  T. Due

to hysteresis effects the saturation fields along b depend on the sweep direction with  $B_b^s = +0.45 \pm 0.01$  T and  $B_b^s = -0.37 \pm 0.01$  T. The energy shift for sweeps along the a-axis follows a stronger curvature with applied field compared to sweeps along the c-axis [35].

The continuous energy shift of the emission peaks for sweeps along the magnetic hard and intermediate axis allows the assignment of the emission peaks in the AFM and FM state, which we aim to identify. For comparison, the abrupt jumps at  $B_b^s$  make peak assignments between optical emission in the AFM and FM states more challenging. In our PL measurements, the linear excitation polarization is aligned with the crystal a-axis, while the detection polarization is aligned with the b-axis (see Figure 1 b). The crystal axes were determined via the maximum and minimum PL intensity for the b-axis and a-axis respectively. Figure 2 a and b show the polarization dependence of the PL emission of encapsulated 14 layer CrSBr at  $B = 0$  T. Due to the strong anisotropy of the material, the PL emission is highly linearly polarized exhibiting maximum intensity along the b-axis and about a factor of 200 weaker intensity along the a-axis. Both samples show qualitatively similar PL spectra with a multitude of different emission peaks with narrow linewidths (of the order of meV) as shown in Figure 2 a

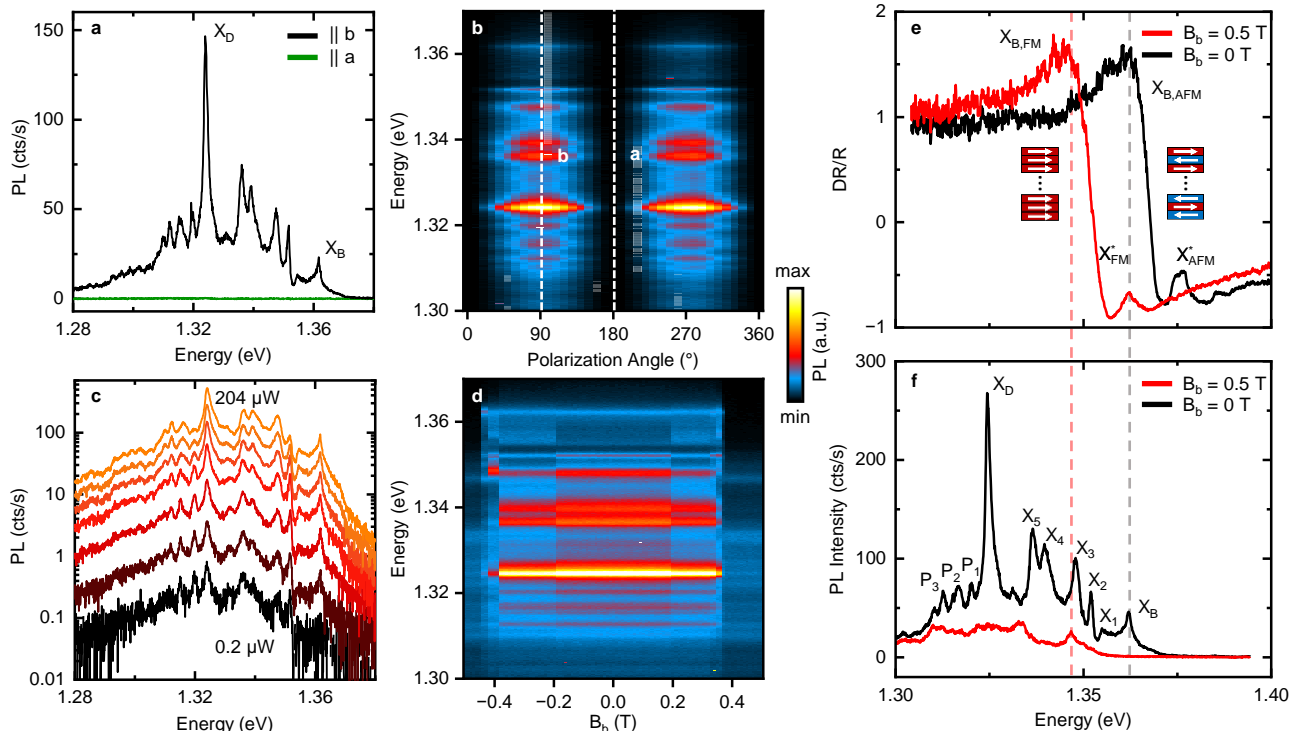


FIG. 2: **Photoluminescence and differential reflectance contrast of encapsulated 14 layer CrSBr at  $T = 4.7$  K.** a: PL spectra at  $B = 0$  T with detection polarization aligned with the crystal b- (black solid line) and a-axis (green solid line). b: Full polarization dependence of the emission. c: Power dependence of the PL emission at  $B = 0$  T. d: PL magnetic field sweeps along the crystal b-axis for an encapsulated (14 L) sample. Magnetic field step size is 10 mT, sweep direction from positive to negative fields. e-f: DR/R and PL spectra of the 14 layer sample for the AFM-state (black) and the FM-state (red). Emissions indicated as in main text. Dashed gray and red lines indicate the energy of  $X_B$  in the AFM and FM state respectively.

for encapsulated 14 layer and in 6 a for unencapsulated 10 layer CrSBr. Importantly, due to the small sample thickness, the rich spectra cannot stem from polaritonic states, as reported for bulk CrSBr layers [18, 19], but from different excitonic species and their phonon replica, which we aim to identify further.

In Figure 2 a, we mark two transitions, that will be of significance in our discussion. The transition  $X_D$ , which is the strongest in PL and the transition  $X_B$ , which is visible in PL and is the strongest transition in terms of oscillator strength in DR/R, see below. Observing strong PL from transitions that have low oscillator strength resembles the rich PL spectra of WSe<sub>2</sub> monolayers with several exciton species [36–38].

We performed excitation power dependent measurements, displayed in Figure 2 c, to ensure, that we capture all details of the complex spectra. Since the spectra in the investigated power range experience only slight changes in their relative intensities, we continue with a moderate excitation power of about 60  $\mu$ W. In the unencapsulated sample, the changes from low to high power are more pronounced as shown in Figure 6 b. Here we focus on a low excitation power regime, in which both samples

exhibit similar emission properties as highlighted in the direct comparison in Figure 6 a. We note, that the emission peaks in the unencapsulated sample are blueshifted by 4 meV with respect to the encapsulated sample, most likely due dielectric screening [39, 40], while relative energy splittings within the spectra remain unchanged.

Theoretical calculations predict two conduction bands resulting in two possible transitions to the valence band of which one is parity allowed and one is parity forbidden [25, 27]. The notion of parity allowed and forbidden transitions only strictly holds for transitions at very specific points in k-space, which is not fully applicable to the more extended exciton states in CrSBr [41]. As proposed in other work [25, 42], we refer to the emission around 1.362 eV ( $X_B$ ) to the parity allowed transition. This is in accordance with DR/R measurements displayed in Figure 2 e, which reveal an optical resonance with large oscillator strength at the same energy. This resonance is accompanied by a much weaker resonance roughly 14 meV above this transition (see transition labeled  $X^*$  in Figure 5 e). Klein et al. [27] suggest that this resonance might have contributions from the same conduction band along the  $\Gamma - X$  direction. In the PL measurements shown the emission of this transition is absent due to the low excitation power. For the

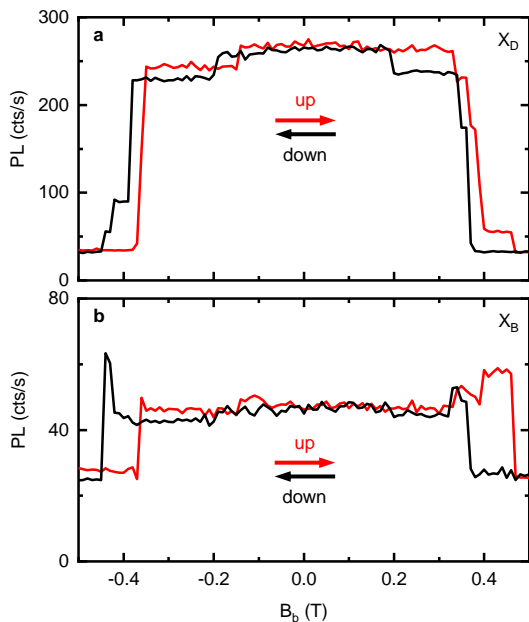


FIG. 3: **Hysteresis of PL intensities in magnetic fields along  $B_b$ .** a-b: Maximum intensity plots of  $X_D$  (a) and  $X_B$  (b) for the encapsulated 14L sample for up-sweeping (down-sweeping) magnetic field in red (black).

assignment of the so-called parity forbidden transition  $X_D$ , we refer to work by Lin et al. [15, 42]. This corresponds to the brightest transition in PL emission located around 1.324 eV, 38 meV below  $X_B$  in agreement with previous reports and theoretical predictions for the splitting of the exciton energies [25, 42]. We note, that the magnitude of the bandgap energy and the origin and magnitude of the splitting between  $X_B$  and  $X_D$  is discussed in several studies [27, 30, 43–46]. Our work is adding contrasting magnetic field effects to the observed distinctions between the two transitions. Importantly, we do not observe any signature of  $X_D$  in DR/R in agreement with its parity forbidden character i.e. predicted weak oscillator strength. Between  $X_B$  and  $X_D$  we find several emission peaks, that we label  $X_{1-5}$  as well as three emissions below  $X_D$ , which we label  $P_{1-3}$ .

To gain further insight into the origin of the emission peaks  $X_{1-5}$  and  $P_{1-3}$ , we performed magnetic field sweeps along the magnetic easy axis (for details see methods). We recorded a full hysteresis loop starting in the FM state at negative magnetic field  $B_b$  and focus on the down-sweep direction of the measurement loop shown in Figure 2 d. Figure 3 displays the maximum intensity of  $X_D$  and  $X_B$  for the whole magnetic field sweep including strong hysteresis effects. For both samples, we observe several abrupt changes in the emission intensities at distinctly different magnetic fields. Hence, the magnetization of the sample changes in discrete steps, i.e. different layers in the sample change their spin orientation individually. We note a certain analogy to layer by layer

switching in Fe/MgO (001) superlattices [47], albeit we use here simple PL and DR/R measurements to monitor the magnetism in CrSBr. Importantly, different PL emission peaks change at the same magnetic field demonstrating the strong coupling of excitons to the magnetic order of the system. The emission changes most drastically, when the magnetic field reaches the saturation field and the remaining layers of the system switch to the FM state. For the down-sweep direction in Figure 2 d, this happens at  $B_b < -0.44$  T in the encapsulated sample. In the unencapsulated sample, the switch happens at  $B_b < -0.37$  T. Due to hysteresis, the FM state starts to vanish at a different field  $B_b < 0.38$  T in the encapsulated sample and  $B_b < 0.36$  T in the unencapsulated sample. In the FM state, the emission intensity is much weaker than in the antiferromagnetic (AFM) state and the emissions experience a redshift of 16 meV for  $X_B$  and 14 meV for  $X_D$ . This reduction of intensity is thought to result from the reduced layer confinement of excitons in the FM state [48]. In the AFM state, the antiparallel magnetization of adjacent layers does not allow charge transfer between layers and thus excitons are confined to a layer. However, the parallel magnetization of adjacent layers in the FM state allows charge transfer reducing the electron-hole wavefunction overlap. Strikingly, all emission peaks in the investigated samples are weaker in the FM states while the exact changes during the transition can differ which we will elaborate further. In the FM state, the intensity of  $X_B$  and  $X_D$  reduce by approximately  $46 \pm 3\%$  and  $88 \pm 1\%$  respectively.

We now turn to a more detailed discussion of the emission changes. Figure 4 a and b display spectra recorded at different values of  $B_b$  in a spectral range around the strongest peak in PL emission  $X_D$ . With increasing magnetic field strength, all of the emission peaks in this range reduce in intensity until either vanishing (within our detection limit) or experiencing an energy shift at the switch to the FM phase. A moderate reduction in intensity appears at  $B_b = \pm 0.2$  T, which likely corresponds to a switch of an individual layer magnetization. Figure 4 c (for transitions  $X_D, X_4, X_5$ ) and d (for transitions  $P_1, P_2, P_3$ ) highlight the collective change, where we plot the maximum intensity of each of the emissions. We emphasize this further by plotting the intensity ratios of the emissions compared to the emission of  $X_D$  in Figure 4 e and f. Until the switching to the fully ferromagnetic phase, the intensity ratios stay almost constant. We want to emphasize that in addition, before reaching  $B_b^S$  none of these emissions exhibit an energy shift despite the changes in intensity. Due to this correlated behaviour, these emissions might stem from the same band transition.

The emissions  $P_1, P_2$  and  $P_3$  are redshifted with respect to  $X_D$  by 4.2 meV, 7.8 meV and 11.8 meV respectively, i.e. approximately equidistantly spaced by 4 meV. From this one might speculate, that the emissions  $P_1, P_2$  and  $P_3$  are phonon replica of  $X_D$ . Pawbake et al. [49]

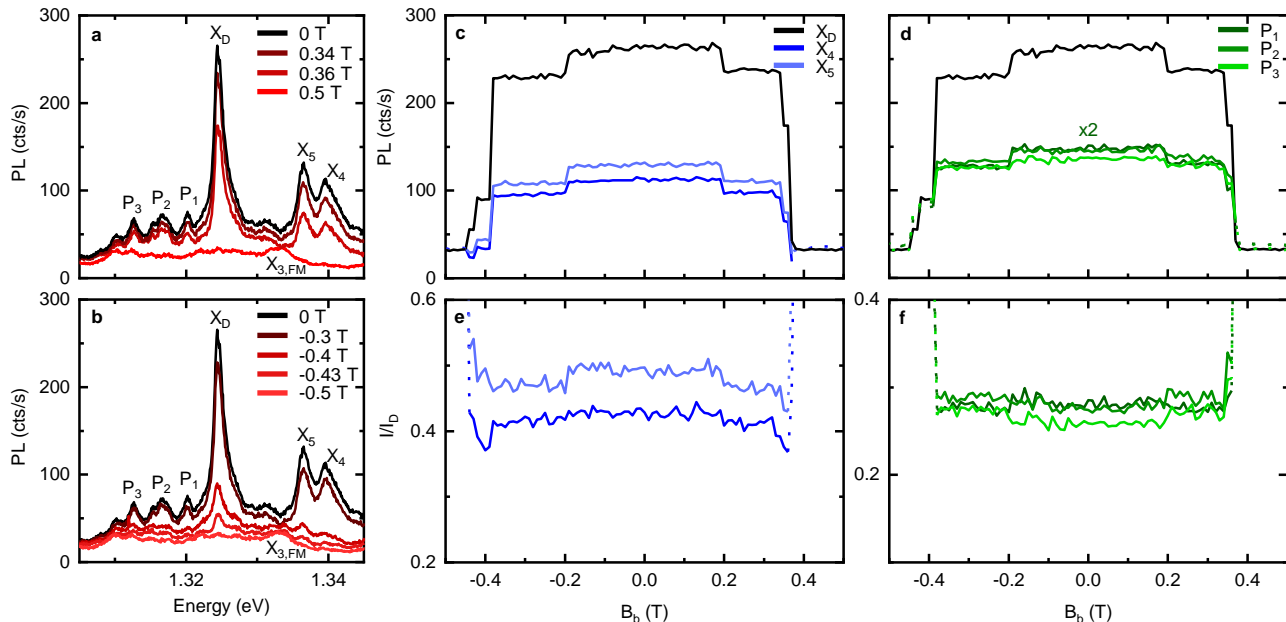


FIG. 4: **Correlated emissions in magnetic fields.** a: PL emission of the encapsulated CrSBr flake for selected magnetic field strengths  $B_b$  along the crystal b-axis and spectral range displaying similar and consistent reduction of emission intensity with magnetic field. b: same as (a), but for negative magnetic fields. Gray arrow is a guide for the eye. c-d: Maximum intensity of the emissions marked in (a) for the magnetic field sweep in Figure 2 d. e-f: Maximum emission intensity in c-d normalized by the intensity of  $X_D$ . Pointed parts of the graphs indicate regions with large error bars.

report, that the increased size of the unit cell in the AFM phase leads to backfolding of several phonon modes to the  $\Gamma$ -point compared to the FM phase. Consequently, several acoustic phonon modes in the energy range of 20-40  $\text{cm}^{-1}$  (2.5 - 5 meV) could in principle couple to the exciton and create the observed equidistant emissions. In the FM phase, these phonon modes would gain finite quasi-momentum and thus the replica would disappear again. Within the resolution of the observed PL spectra we cannot identify the presence of  $P_{1-3}$  in the FM phase. We note, that in the energy range of  $P_{1-3}$  phonon replica of  $X_D$  with the  $A_g^1$  mode have been reported [15]. At higher excitation powers, we find signatures of these emissions overlaid with  $P_{1-3}$ . The attribution of  $X_4$  and  $X_5$ , centered around 1.340 eV and 1.337 eV respectively, need to be clarified in further studies. At this point we can report that  $X_4$  and  $X_5$  show an evolution with magnetic field  $B_b$ , that is similar to  $X_D$ .

While the emission peaks between 1.31 eV and 1.345 eV experience very similar emission changes in magnetic fields compared to  $X_D$ , the emissions between 1.345 eV and 1.37 eV behave very differently. Figure 5 a and b show spectra in this energy range for the same magnetic field values as in Figure 4 a and b. At zero magnetic field, the emission energies of  $X_{1-3}$  are located at  $E_1 = 1.355$  eV,  $E_2 = 1.352$  eV and  $E_3 = 1.348$  eV. Most strikingly, the intensity of  $X_B$  as a function of  $B_b$  evolves very differently compared to  $X_D$ , as

highlighted in Figure 5 c and comparing Figures 3 a and b. As described before, the intensity of  $X_D$  reduces measurably as individual layers flip spin orientation. In contrast, the intensity of  $X_B$  reduces less as highlighted in Figure 5 c. Very surprisingly, at magnetic fields close to the transition to the FM state, the intensity of  $X_B$  increases. Similar to  $X_B$ , also the transitions  $X_1$ ,  $X_2$  and  $X_3$  experience an increase in intensity close to the saturation field. Additionally,  $X_2$  and  $X_3$  initially decrease in intensity with the single layer switch at  $B_b = \pm 0.2$  T. In contrast, at  $B_b = \pm 0.2$  T the transition  $X_1$  increases its intensity. Despite the changes,  $X_B$  and  $X_2$  do not shift in energy before the transition to the FM state. However,  $X_1$  and  $X_3$  experience a slight blueshift as shown in Figure 5 a and b.

Above  $B_b^S$  the entire crystal is in the FM state. For applied magnetic fields  $0 < B_{\text{applied}} < B_b^S$  the AFM and FM configuration can coexist in the crystal and we observe spectral features of both configurations in PL and DR/R measurements. In PL, the emission peak of e.g.  $X_{3,FM}$  is overlaid with the weakened emission peaks of  $X_4$  and  $X_5$  in the AFM configuration as highlighted in Figure 4 b. Similarly, the emission peak of  $X_{B,FM}$  is overlaid with the emission peak of  $X_3$  displayed in Figure 5 a and b. Further insight comes from DR/R measurements at magnetic fields close to the transition displayed in Figure 5 e. In addition to resonance of  $X_{B,AFM}$ , another resonance appears at 1.347 eV, which we identify as the resonance of  $X_B$

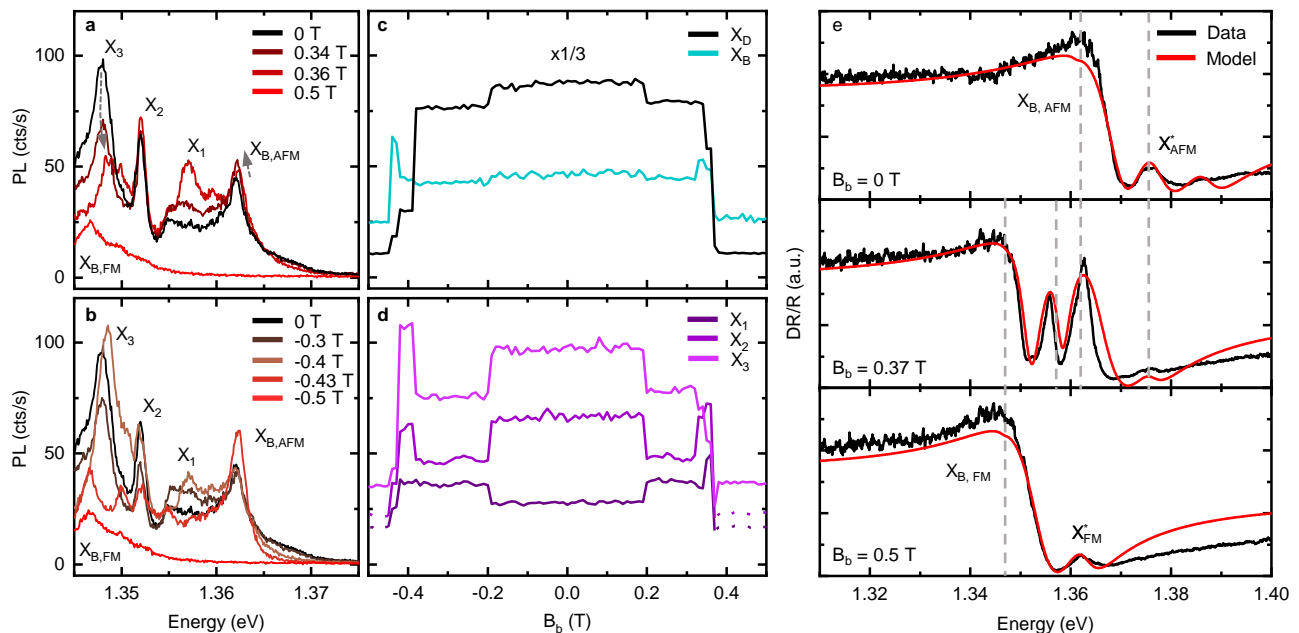


FIG. 5: **Anti-correlated emissions and superimposed magnetic phases.** a: PL emission for selected magnetic field strengths and spectral range along the crystal b-axis showing unexpected brightening of emissions. b: same as (a), but for negative magnetic fields. Grey arrows are guides for the eye. c: Maximum intensity of the  $X_B$  and  $X_D$  emissions for magnetic field sweep in Figure 2 d.  $X_D$  ( $X_B$ ) reduces in intensity by  $9.5 \pm 2\%$  ( $4.1 \pm 4\%$ ) for  $B_b > 0.18$  T and by  $12.3 \pm 2\%$  ( $8.1 \pm 4.2\%$ ) for  $B_b < -0.2$  T. d: Maximum intensity of the remaining emissions marked in (a). Pointed parts of the graphs indicate regions with large error bars. e: Transfer-matrix-analysis of DR/R measurements for selected magnetic fields. Dashed grey lines indicate the energies of the respective oscillators.

in the FM state ( $X_{B,FM}$ ). The resonance of  $X_{B,FM}$  appears several 10 mT below the saturation field and persists above it. Surprisingly, the measurements reveal an additional resonance at 1.357 eV, redshifted by 5 meV from  $X_{B,AFM}$  around 1.362 eV, as shown in Figure 5 e. This resonance appears with the first switch of magnetization and remains present until the system fully transitions into the FM state, where it vanishes. The origin of this resonance remains to be clarified. We use a transfer-matrix-analysis (for details see methods) to reconstruct the measurements and determine the resonance energies of the oscillators present in the different magnetic phases. This analysis is necessary as the resonance energies do not coincide with extrema of the DR/R spectra due to interference effects and the finite thickness of the CrSBr layers. We are able to reproduce the spectra well with our formalism allowing to determine the resonance energies present in the spectrum with an estimated accuracy of 1-2 meV. For consistency, we checked the unencapsulated sample in several spots and it exhibits a similar superposition of the individual resonances as highlighted in Figure 7.

*In conclusion*, tuning the magnetic field in a three-axis vector magnet gives access to the different spin configurations in multilayer CrSBr. Photoluminescence measurements reveal step-like changes in intensity for all observed emission peaks correlated to a layer by layer switching of

the magnetization for fields applied along the magnetic easy axis. Some of these emissions around the parity forbidden transition  $X_D$  reduce monotonously with increasing magnetic field and do not experience energy shifts until the saturation field along  $B_b$ . We find several exceptions from this trend between  $X_D$  and  $X_B$ , that do experience energy shifts and even increase in intensity close to the saturation field. Additionally, we find, that in phases close to the transition to the FM state, excitonic emission from the AFM and FM phases coexists. We show that the comparison between PL and reflectivity measurements gives access to the magnetization configurations within the multilayer.

### III. METHODS

#### A. Sample fabrication:

Bulk CrSBr crystals were fabricated through chemical vapor transport [50]. Nanometer thin CrSBr and hBN flakes were mechanically exfoliated onto PDMS and transferred onto Si substrates with an 80 nm thick oxide layer. The layer thicknesses were determined using an atomic force microscope (Oxford Instruments Cypher) equipped with AC160 cantilevers (Oxford Instruments). Atomic force microscopy yields CrSBr thickness of  $8.2 \pm 0.3$  nm ( $11.3 \pm 0.2$  nm) corresponding to 10 (14) lay-

ers for the unencapsulated (encapsulated) sample. Both samples were annealed at 200° for several hours.

### B. Optical spectroscopy:

Optical spectroscopy was carried out in a home-built confocal setup for magneto-optical spectroscopy [38]. The sample was placed inside a closed-cycle cryostat (attocube systems, AttoDry 1000XL) equipped with a vector magnet (z-axis: solenoid, maximum field 5 T, x-/y-axis: Split Coil, maximum field 2 T). We used low temperature piezo-positioners (attocube systems, ANPx101 and ANPz102) to position the sample with respect to a low temperature apochromatic objective. PL and DR/R measurements were performed in backscattering geometry at a sample temperature of 4.7 K. The signal was dispersed inside a Czerny-Turner spectrograph (Teledyne Princeton Instruments, SpectraPro HRS-500) and detected by a CCD-camera (Teledyne Princeton Instruments, Pylon BRexcelon 100). For DR/R measurements we used a Tungsten-Halogen lamp (Thorlabs, SLS201L/M) polarized along the crystal b-axis by a nanoparticle-film polarizer and an achromatic half-waveplate. For PL measurements we used a HeNe Laser (Thorlabs, HNL210LB) with its polarization aligned along the crystal a-axis while the emission was detected along the b-axis. PL measurements were performed at excitation powers ranging from 250 nW to 260 μW. Magnetic field dependent measurements were performed initializing the CrSBr sample in the FM-state, ramping the magnet to -0.6 T (-0.5 T) for the encapsulated 14 layers (unencapsulated, 10 layers) sample, followed by a sweep to 0.6 T (0.5 T) and subsequent inversion of the sweep direction to obtain a full hysteresis.

### C. Transfer-matrix analysis

For the analysis of differential reflectance contrast measurements, we apply a transfer-matrix formalism [18, 19, 51], using a Lorentzian oscillator model for the dielectric constant of CrSBr

$$\epsilon(\omega) = \epsilon_\infty + \sum_j \frac{f_j/\hbar^2}{\omega_j^2 - \omega^2 - i\Gamma_j\omega} \quad (1)$$

where  $\omega_j$  and  $\Gamma_j$  denote the oscillator frequency and decay rate and  $f_j$  denotes the oscillator strength of the  $j$ th oscillator. We account for a constant background permittivity  $\epsilon_\infty = 10$ , similar to Wang et al [19] and use the permittivities  $\epsilon_{SiO_2} = 2.1$  [52],  $\epsilon_{Si} = 13$  [53] and  $\epsilon_{hBN} = 4.6$  [54].

#### Acknowledgements:

We thank Florian Dirnberger for fruitful discussions. K.W. and T.T. acknowledge support from the JSPS KAKENHI (Grant Numbers 21H05233 and 23H02052)

, the CREST (JPMJCR24A5), JST and World Premier International Research Center Initiative (WPI), MEXT, Japan. Z.S. was supported by ERC-CZ program (project LL2101) from Ministry of Education Youth and Sports (MEYS) and by the project Advanced Functional Nanorobots (reg. No. CZ.02.1.01/0.0/0.0/15\_003/0000444 financed by the EFRR).

**Author Contributions:** K.M. and Z.S. grew bulk CrSBr crystals. T.T. and K.W. grew bulk hBN crystals. L.K. fabricated the samples and performed optical spectroscopy with R.T.. P.M., L.K., K.H., R.v.K. performed and analysed AFM measurements. L.K., R.T. and B.U. analyzed the optical spectra. L.K., R.T., P.M., D.M. and B.U. discussed the results. B.U. suggested the experiments and supervised the project. L.K., R.T. and B.U. wrote the manuscript. All authors contributed to the final manuscript.

**Competing interests:** The authors declare no competing interests.

### REFERENCES

- [1] M. Gibertini, M. Koperski, A. F. Morpurgo, and K. S. Novoselov, *Nature nanotechnology* **14**, 408 (2019).
- [2] T. Song, X. Cai, M. W.-Y. Tu, X. Zhang, B. Huang, N. P. Wilson, K. L. Seyler, L. Zhu, T. Taniguchi, K. Watanabe, et al., *Science* **360**, 1214 (2018).
- [3] Z. Wang, I. Gutiérrez-Lezama, N. Ubrig, M. Kroner, M. Gibertini, T. Taniguchi, K. Watanabe, A. Imamoğlu, E. Giannini, and A. F. Morpurgo, *Nature communications* **9**, 2516 (2018).
- [4] E. C. Ahn, *npj 2D Materials and Applications* **4**, 17 (2020).
- [5] M. Mi, H. Xiao, L. Yu, Y. Zhang, Y. Wang, Q. Cao, and Y. Wang, *Materials Today Nano* p. 100408 (2023).
- [6] Y. Liu, W. Wang, H. Lu, Q. Xie, L. Chen, H. Yin, G. Cheng, and X. Wu, *Applied Surface Science* **511**, 145452 (2020).
- [7] M. Galbiati, V. Zatzko, F. Godel, P. Hirschauer, A. Vecchiola, K. Bouzehouane, S. Collin, B. Servet, A. Cantarero, F. Petroff, et al., *ACS Applied Electronic Materials* **2**, 3508 (2020).
- [8] J. T. Gish, D. Lebedev, T. K. Stanev, S. Jiang, L. Georgopoulos, T. W. Song, G. Lim, E. S. Garvey, L. Valdman, O. Balogun, et al., *ACS nano* **15**, 10659 (2021).
- [9] D. Shcherbakov, P. Stepanov, D. Weber, Y. Wang, J. Hu, Y. Zhu, K. Watanabe, T. Taniguchi, Z. Mao, W. Windl, et al., *Nano letters* **18**, 4214 (2018).
- [10] M. E. Ziebel, M. L. Feuer, J. Cox, X. Zhu, C. R. Dean, and X. Roy, *Nano Letters* **24**, 4319 (2024).
- [11] C. Ye, C. Wang, Q. Wu, S. Liu, J. Zhou, G. Wang, A. Soll, Z. Sofer, M. Yue, X. Liu, et al., *ACS nano* **16**, 11876 (2022).
- [12] Y. J. Bae, J. Wang, A. Scheie, J. Xu, D. G. Chica, G. M. Diederich, J. Cenker, M. E. Ziebel, Y. Bai, H. Ren, et al., *Nature* **609**, 282 (2022).

- [13] G. M. Diederich, J. Cenker, Y. Ren, J. Fonseca, D. G. Chica, Y. J. Bae, X. Zhu, X. Roy, T. Cao, D. Xiao, et al., *Nature Nanotechnology* **18**, 23 (2023).
- [14] G. M. Diederich, M. Nguyen, J. Cenker, J. Fonseca, S. Pumulo, Y. J. Bae, D. G. Chica, X. Roy, X. Zhu, D. Xiao, et al., arXiv preprint [arXiv:2411.14943](https://arxiv.org/abs/2411.14943) (2024).
- [15] K. Lin, X. Sun, F. Dirnberger, Y. Li, J. Qu, P. Wen, Z. Sofer, A. Söll, S. Winnerl, M. Helm, et al., *ACS nano* **18**, 2898 (2024).
- [16] P. Mondal, D. I. Markina, L. Hopf, L. Krelle, S. Shradha, J. Klein, M. M. Glazov, I. Gerber, K. Hagmann, R. v. Klitzing, et al., arXiv preprint [arXiv:2410.22164](https://arxiv.org/abs/2410.22164) (2024).
- [17] S. Sahu, C. Berrezueta-Palacios, S. Juergensen, K. Mosina, Z. Sofer, M. Velický, P. Kusch, and O. Frank, arXiv preprint [arXiv:2502.01794](https://arxiv.org/abs/2502.01794) (2025).
- [18] F. Dirnberger, J. Quan, R. Bushati, G. M. Diederich, M. Florian, J. Klein, K. Mosina, Z. Sofer, X. Xu, A. Kamra, et al., *Nature* **620**, 533 (2023).
- [19] T. Wang, D. Zhang, S. Yang, Z. Lin, Q. Chen, J. Yang, Q. Gong, Z. Chen, Y. Ye, and W. Liu, *Nature Communications* **14**, 5966 (2023).
- [20] C. Li, C. Shen, N. Jiang, K. K. Tang, X. Liu, J. Guo, Y. Liang, J. Song, X. Deng, and Q. Zhang, *Advanced Functional Materials* p. 2411589 (2024).
- [21] L. Nessi, C. A. Occhialini, A. K. Demir, L. Powalla, and R. Comin, *ACS nano* (2024).
- [22] B. Han, H. Shan, K. W. Song, L. Lackner, M. Esmann, V. Solovyeva, F. Eilenberger, J. Regner, Z. Sofer, O. Kyriienko, et al., arXiv preprint [arXiv:2501.18233](https://arxiv.org/abs/2501.18233) (2025).
- [23] C. Boix-Constant, S. Mañas-Valero, A. M. Ruiz, A. Rybakov, K. A. Konieczny, S. Pillet, J. J. Baldoví, and E. Coronado, *Advanced Materials* **34**, 2204940 (2022).
- [24] E. J. Telford, A. H. Dismukes, K. Lee, M. Cheng, A. Wieteska, A. K. Bartholomew, Y.-S. Chen, X. Xu, A. N. Pasupathy, X. Zhu, et al., *Advanced Materials* **32**, 2003240 (2020).
- [25] N. P. Wilson, K. Lee, J. Cenker, K. Xie, A. H. Dismukes, E. J. Telford, J. Fonseca, S. Sivakumar, C. Dean, T. Cao, et al., *Nature Materials* **20**, 1657 (2021).
- [26] F. Tabataba-Vakili, H. P. Nguyen, A. Rupp, K. Mosina, A. Papavasileiou, K. Watanabe, T. Taniguchi, P. Maletinsky, M. M. Glazov, Z. Sofer, et al., *Nature Communications* **15**, 4735 (2024).
- [27] J. Klein, B. Pingault, M. Florian, M.-C. Heißenbüttel, A. Steinhoff, Z. Song, K. Torres, F. Dirnberger, J. B. Curtis, M. Weile, et al., *ACS nano* **17**, 5316 (2023).
- [28] K. Yang, G. Wang, L. Liu, D. Lu, and H. Wu, *Physical Review B* **104**, 144416 (2021).
- [29] M. Liebich, M. Florian, N. Nilforoushan, F. Mooshammer, A. Koulouklidis, L. Wittmann, K. Mosina, Z. Sofer, F. Dirnberger, M. Kira, et al., *Nature Materials* (2025).
- [30] Y. Shao, F. Dirnberger, S. Qiu, S. Acharya, S. Terres, E. J. Telford, D. Pashov, B. S. Kim, F. L. Ruta, D. G. Chica, et al., *Nature materials* (2025).
- [31] M. A. Tschudin, D. A. Broadway, P. Siegwolf, C. Schrader, E. J. Telford, B. Gross, J. Cox, A. E. Dubois, D. G. Chica, R. Rama-Eiroa, et al., *Nature Communications* **15**, 6005 (2024).
- [32] D. J. Rizzo, A. S. McLeod, C. Carnahan, E. J. Telford, A. H. Dismukes, R. A. Wiscons, Y. Dong, C. Nuckolls, C. R. Dean, A. N. Pasupathy, et al., *Advanced Materials* **34**, 2201000 (2022).
- [33] K. Lee, A. H. Dismukes, E. J. Telford, R. A. Wiscons, J. Wang, X. Xu, C. Nuckolls, C. R. Dean, X. Roy, and X. Zhu, *Nano Letters* **21**, 3511 (2021).
- [34] O. Göser, W. Paul, and H. Kahle, *Journal of magnetism and magnetic materials* **92**, 129 (1990).
- [35] M.-C. Heißenbüttel, P.-M. Piel, J. Klein, T. Deilmann, U. Wurstbauer, and M. Rohlfing, *Phys. Rev. B* **111**, 075107 (2025).
- [36] G. Wang, C. Robert, M. M. Glazov, F. Cadiz, E. Courtade, T. Amand, D. Lagarde, T. Taniguchi, K. Watanabe, B. Urbaszek, et al., *Physical review letters* **119**, 047401 (2017).
- [37] M. He, P. Rivera, D. Van Tuan, N. P. Wilson, M. Yang, T. Taniguchi, K. Watanabe, J. Yan, D. G. Mandrus, H. Yu, et al., *Nature communications* **11**, 618 (2020).
- [38] S. Shree, I. Paradisanos, X. Marie, C. Robert, and B. Urbaszek, *Nature Reviews Physics* **3**, 39 (2021).
- [39] A. Raja, A. Chaves, J. Yu, G. Arefe, H. M. Hill, A. F. Rigosi, T. C. Berkelbach, P. Nagler, C. Schüller, T. Korn, et al., *Nature communications* **8**, 15251 (2017).
- [40] A. V. Stier, N. P. Wilson, G. Clark, X. Xu, and S. A. Crooker, *Nano letters* **16**, 7054 (2016).
- [41] M. Bianchi, S. Acharya, F. Dirnberger, J. Klein, D. Pashov, K. Mosina, Z. Sofer, A. N. Rudenko, M. I. Katsnelson, M. Van Schilfgaarde, et al., *Physical Review B* **107**, 235107 (2023).
- [42] K. Lin, Y. Li, M. Ghorbani-Asl, Z. Sofer, S. Winnerl, A. Erbe, A. V. Krashennnikov, M. Helm, S. Zhou, Y. Dan, et al., *The Journal of Physical Chemistry Letters* **15**, 6010 (2024).
- [43] R. Komar, A. Łopion, M. Goryca, M. Rybak, T. Woźniak, K. Mosina, A. Söll, Z. Sofer, W. Pacuski, C. Faugeras, et al., arXiv preprint [arXiv:2409.00187](https://arxiv.org/abs/2409.00187) (2024).
- [44] S. Smolenski, M. Wen, Q. Li, E. Downey, A. Alfrey, W. Liu, A. L. Kondusamy, A. Bostwick, C. Jozwiak, E. Rotenberg, et al., *Nature Communications* **16**, 1134 (2025).
- [45] T.-X. Qian, J. Zhou, T.-Y. Cai, and S. Ju, *Physical Review Research* **5**, 033143 (2023).
- [46] B. Datta, P. C. Adak, S. Yu, A. V. Dharmapalan, S. J. Hall, A. Vakulenko, F. Komissarenko, E. Kurganov, J. Quan, W. Wang, et al., arXiv preprint [arXiv:2409.18501](https://arxiv.org/abs/2409.18501) (2024).
- [47] R. Moubah, F. Magnus, T. Warnatz, G. K. Pálsson, V. Kapaklis, V. Ukleev, A. Devishvili, J. Palisaitis, P. Persson, and B. Hjörvarsson, *Physical Review Applied* **5**, 044011 (2016).
- [48] F. Marques-Moros, C. Boix-Constant, S. Mañas-Valero, J. Canet-Ferrer, and E. Coronado, *ACS nano* **17**, 13224 (2023).
- [49] A. Pawbake, T. Pelini, N. P. Wilson, K. Mosina, Z. Sofer, R. Heid, and C. Faugeras, *Physical Review B* **107**, 075421 (2023).
- [50] J. Klein, T. Pham, J. Thomsen, J. Curtis, T. Denneulin, M. Lorke, M. Florian, A. Steinhoff, R. Wiscons, J. Luxa, et al., *Nature Communications* **13**, 5420 (2022).
- [51] C. Robert, M. Semina, F. Cadiz, M. Manca, E. Courtade, T. Taniguchi, K. Watanabe, H. Cai, S. Tongay, B. Lassagne, et al., *Physical Review Materials* **2**, 011001 (2018).
- [52] I. H. Malitson, *Journal of the optical society of America* **55**, 1205 (1965).
- [53] C. Schinke, P. Christian Peest, J. Schmidt, R. Brendel, K. Bothe, M. R. Vogt, I. Kröger, S. Winter, A. Schirma-



cher, S. Lim, et al., *Aip Advances* **5** (2015).  
[54] S.-Y. Lee, T.-Y. Jeong, S. Jung, and K.-J. Yee, *physica*

*status solidi (b)* **256**, 1800417 (2019).

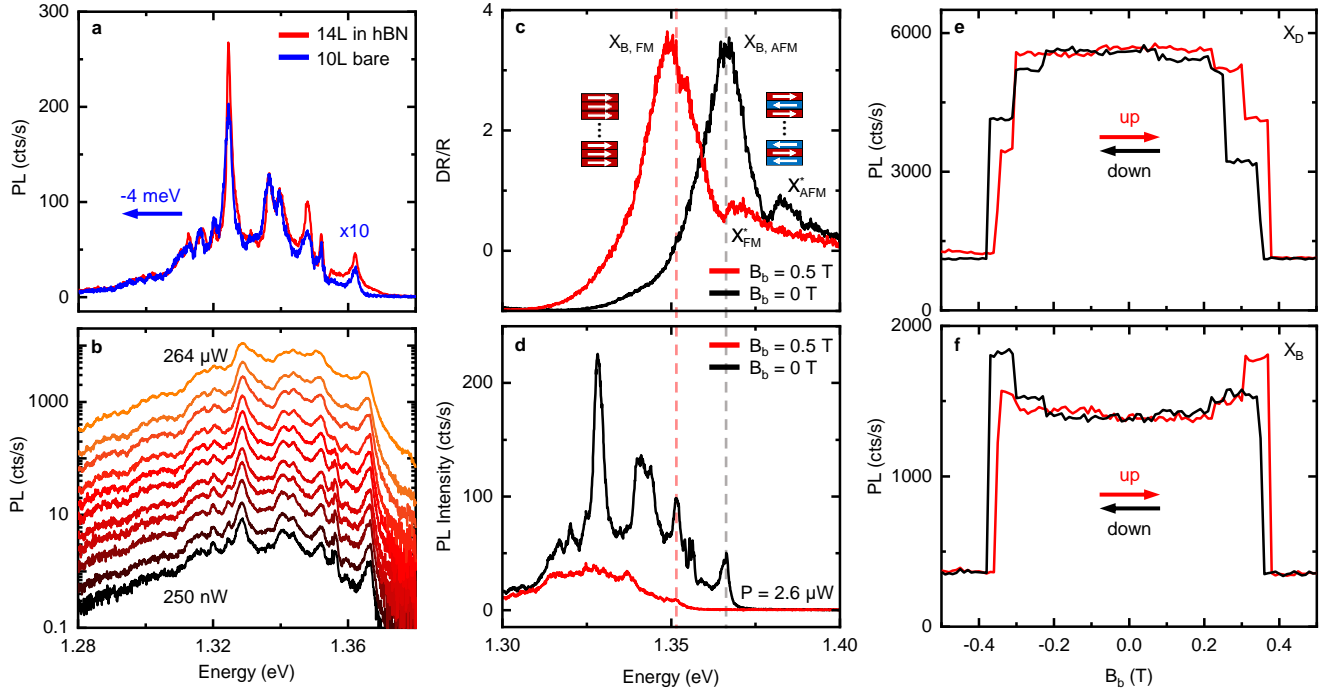


FIG. 6: **Characteristics of the unencapsulated 10L sample.** a: PL comparison of the two samples. Excitation power was  $77.6 \mu\text{W}$  for the encapsulated sample and  $250 \text{ nW}$  for the unencapsulated sample. The spectrum of the unencapsulated sample was redshifted by  $4 \text{ meV}$  for better comparison. b: Powerdependence of the PL emission. c-d: DR/R and PL for the AFM (black) and FM (red) phase. Dashed gray and red lines indicate the energy of  $X_B$  in the AFM and FM state respectively. e-f: Maximum intensity plots of  $X_D$  (e) and  $X_B$  (f) for the unencapsulated 10L sample for up-sweeping (down-sweeping) magnetic field in red (black).

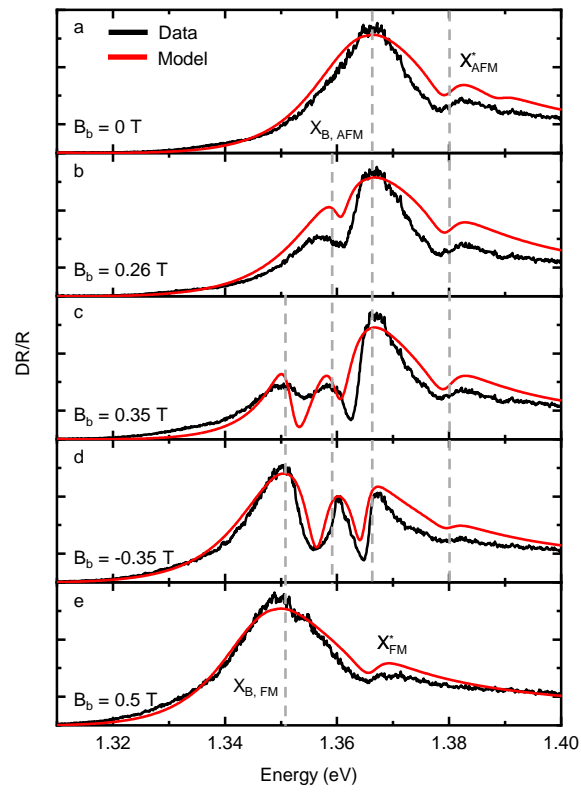


FIG. 7: Transfer-matrix-analysis of DR/R measurements of the unencapsulated 10L sample for selected magnetic fields. Dashed lines indicate the energies of the respective oscillators.